
Since January 2020 Elsevier has created a COVID-19 resource centre with free information in English and Mandarin on the novel coronavirus COVID-19. The COVID-19 resource centre is hosted on Elsevier Connect, the company's public news and information website.

Elsevier hereby grants permission to make all its COVID-19-related research that is available on the COVID-19 resource centre - including this research content - immediately available in PubMed Central and other publicly funded repositories, such as the WHO COVID database with rights for unrestricted research re-use and analyses in any form or by any means with acknowledgement of the original source. These permissions are granted for free by Elsevier for as long as the COVID-19 resource centre remains active.

Journal of Pharmaceutical and Biomedical Analysis 206 (2021) 114392

Contents lists available at ScienceDirect

Journal of Pharmaceutical and Biomedical Analysis

journal homepage: www.elsevier.com/locate/jpba

# Nanostructured sensor platform based on organic polymer conjugated to metallic nanoparticle for the impedimetric detection of SARS-CoV-2 at various stages of viral infection

Karen Y.P.S. Avelino[a,b], Giselle S. dos Santos[a,b], Isaac A.M. Frías[a,b], Alberto G. Silva-Junior[a,b], Michelly C. Pereira[c], Maira G.R. Pitta[c], Breno C. de Araújo[c], Abdelhamid Errachid[d], Maria D.L. Oliveira[a,b], César A.S. Andrade[a,b,*]

[a] Programa de Pós-Graduação em Inovação Terapêutica, Universidade Federal de Pernambuco, 50670–901 Recife, PE, Brazil
[b] Laboratório de Biodispositivos Nanoestruturados, Departamento de Bioquímica, Universidade Federal de Pernambuco, 50670–901 Recife, PE, Brazil
[c] Laboratório de Imunomodulação e Novas Abordagens Terapêuticas, Núcleo de Pesquisa em Inovação Terapêutica, Universidade Federal de Pernambuco, 50670–901 Recife, PE, Brazil
[d] Université Claude Bernard Lyon 1, Institut des Sciences Analytiques (ISA), 5 rue de la Doua, 69100, Lyon, Villeurbane, France

ARTICLE INFO

*Article history:*
Received 7 July 2021
Received in revised form 21 September 2021
Accepted 22 September 2021
Available online 24 September 2021

*Keywords:*
Nanostructured biosensor
COVID-19
SARS-CoV-2
Polypyrrole
Gold nanoparticle
Impedance spectroscopy

ABSTRACT

The projection of new biosensing technologies for genetic identification of SARS-COV-2 is essential in the face of a pandemic scenario. For this reason, the current research aims to develop a label-free flexible biodevice applicable to COVID-19. A nanostructured platform made of polypyrrole (PPy) and gold nanoparticles (GNP) was designed for interfacing the electrochemical signal in miniaturized electrodes of tin-doped indium oxide (ITO). Oligonucleotide primer was chemically immobilized on the flexible transducers for the biorecognition of the nucleocapsid protein (N) gene. Methodological protocols based on cyclic voltammetry (CV), electrochemical impedance spectroscopy (EIS), and atomic force microscopy (AFM) were used to characterize the nanotechnological apparatus. The biosensor's electrochemical performance was evaluated using the SARS-CoV-2 genome and biological samples of cDNA from patients infected with retrovirus at various disease stages. It is inferred that the analytical tool was able to distinguish the expression of SARS-CoV-2 in patients diagnosed with COVID-19 in the early, intermediate and late stages. The biosensor exhibited high selectivity by not recognizing the biological target in samples from patients not infected with SARS-CoV-2. The proposed sensor obtained a linear response range estimated from 800 to 4000 copies $\mu L^{-1}$ with a regression coefficient of 0.99, and a detection limit of 258.01 copies $\mu L^{-1}$. Therefore, the electrochemical biosensor based on flexible electrode technology represents a promising trend for sensitive molecular analysis of etiologic agent with fast and simple operationalization. In addition to early genetic diagnosis, the biomolecular assay may help to monitor the progression of COVID-19 infection in a novel manner.

© 2021 Elsevier B.V. All rights reserved.

## 1. Introduction

At the end of 2019, Wuhan province (Hubei, China) reported atypical clinical cases showing similar viral pneumonia symptoms. In January 2020, genome sequencing identified a new coronavirus related to a respiratory disease named SARS-CoV-2, a single-stranded positive-sense RNA virus (+ssRNA), enveloped and shaped like a crown, belonging to the β-coronaviruses genus [1]. An evolutionary analysis concerning 160 complete genomes of SARS-CoV-2 revealed grouping of three central variants characterized by amino acid changes. Its genome revealed three main conserved target sequences i) RNA-dependent RNA polymerase gene (RdRp gene), ii) envelope protein gene (E gene), and iii) nucleocapsid protein gene (N gene). Because of the error rate of its RNA-dependent RNA polymerase (RdRP), mutations and frequent recombination are common, thus accelerating the evolution and adaptation to the host processes [2].

The viral structure consists of 5 proteins, namely: the nucleocapsid protein (N), with the function of packaging the RNA genome;

* Corresponding author at: Departamento de Bioquímica, UFPE, 50670–901, Recife, PE, Brazil.
*E-mail address:* cesar.sandrade@ufpe.br (C.A.S. Andrade).

https://doi.org/10.1016/j.jpba.2021.114392
0731-7085/© 2021 Elsevier B.V. All rights reserved.

membrane proteins (M) that bind to nucleoproteins to form the nucleus structure; the viral envelope consisting of the union of protein M, an envelope protein (E) and spike protein (S), the latter being responsible for facilitating the entry into host cells through receptors such as the angiotensin-converting enzyme 2 (ACE2) abundantly found in lung and small intestine epithelia [3]. According to Iqbal et al., the replication cycle of SARS-CoV-2 involves membrane fusion or endocytosis mechanism; release of viral genome; translation of viral polymerase protein; RNA replication; subgenomic transcription; translation of viral structural protein; viral structural proteins combination with nucleocapsid; formation of mature virion; and release of mature virion via exocytosis mechanism. At this point, the mature virion is enabled to continue the infection of a new target [4].

Human-to-human transmissibility R0 fluctuates but has always been estimated above 1 [5]. Current evidence suggests that its infective efficiency is favored by the inhalation of droplets produced during coughs, speaks, or sneezes and through contact with contaminated fomites. Measurements of infective viral titers have been detected during the asymptomatic incubation period (determined between 1 and 8 days), however after day 8 no isolates were obtained despite ongoing high viral loads. Nevertheless, titers vary according to the patient's medical history, and great caution is advised at all stages to minimize risks [6].

Few distinct stages have been observed in clinical samples from Germany and China during the viral dynamics of SARS-CoV-2. For instance, during the initial stage from day 0 (641 copies $mL^{-1}$), viral titers increase rapidly, reaching a first peak (4–6 days after first symptoms) ranging around $10^4$ to $10^8$ copies $mL^{-1}$. At this point, lymphocyte response is activated, and a plateau phase can be observed. At the last stage, viral titers decline due to the adaptive immune response (after day 8). Nevertheless, some patients present late seroconversion, and therefore viral reinfection and viral persistence are expected [7,8].

The quantitation of viral titers could help to monitor not only the disease's evolution but to evaluate the effect of therapeutic interventions design to tackle SARS-CoV-2 infection. In this context, numeric simulations have shown the effectiveness of combined anti-inflammatory treatments, antiviral drugs and interferon in reducing the duration of the infection's plateau phase and improving the time of recovery [9]. Despite its long response time and relatively complicated operation, real-time quantitative reverse transcription-polymerase chain reaction (qRT-PCR) is the current protagonist method for detecting viral RNA. The minimum laboratory response time is foreseen between 2 and 4 h and may extend up to 1 week if the samples need to be sent to public health laboratories designated by health authorities. Of note, the diagnostic evaluation via qRT-PCR needs to be carried out in certified laboratories with expensive equipment and highly trained technicians. Such limitations hinder the fast and simple diagnosis of suspected patients and monitor infected patients.

With the current information about the multiple biomarkers available to develop molecular and immunological tools to detect SARS-CoV-2 [10], a portable point-of-care test device to identify SARS-CoV-2 could be an excellent alternative to reach marginalized, rural and distant communities. Electrochemical biosensors are known for their sensitivity, specificity and accuracy, and their potential portability and affordability. The measured signal is defined as an increase or a decrease in electrochemical response of the electrode as a result of the target concentration, which is measured either through the electron transfer or the electron transfer resistance.

In this work, we developed a genetic biosensor for the evaluation and monitoring of human SARS-CoV-2 infection. The device can discriminate the early, intermediate, and late infection phases in amplified cDNA patient samples. Conserved SARS-CoV-2 sequences were covalently tethered to an electropolymerized pyrrole-gold nanoparticles (PPy-GNP) transducer, which was used as a working electrode in an electrochemical set-up. In the case of SARS-CoV-2 positive samples, the target sequence will hybridize to the primer, thus inducing the transduction of the biorecognition event into a quantifiable change proportional to its concentration. This platform addresses a key element of traditional nucleic-acid detection assays while reducing the overall cost and achieving low detection limits comparable to qRT-PCR-based tests. Using flexible devices, we combine the portability with sensitivity and selectivity of the detection of SARS-CoV-2 at laboratory-level in biological samples.

## 2. Materials and methods

### 2.1. Reagents and solutions

Tin-doped indium oxide (ITO), pyrrole monomer, tetrachloroauric acid trihydrate ($HAuCl_4.3H_2O$), cysteamine (Cys), potassium ferricyanide ($K_3[Fe(CN)_6]$), potassium ferrocyanide ($K_4[Fe(CN)_6]$), bovine serum albumin (BSA), hydrochloric acid (HCl), glutaraldehyde and sodium phosphate buffer reagents were obtained from Sigma Aldrich (St. Louis, MO, USA). Milli-Q plus water purification system (Millipore, Billerica, USA) was used to obtain deionized water.

### 2.2. Oligonucleotide primers and biological samples

The amino-modified primer was synthesized by Exxtend Biotecnologia Ltda. (Sao Paulo, Brazil). The oligonucleotide sequence (100 pmol $\mu L^{-1}$) was diluted in a Tris-EDTA buffer solution (10 mM and 0.1 mM, respectively) (pH 8). As a positive control, cDNA plasmids with SARS-CoV-2 nucleocapsid gene were used, diluted in a concentration of 200.000 copies $\mu L^{-1}$. To assess the limit of quantification and limit of detection, we prepared a serial dilution of the plasmid control (800–4000 copies $\mu L^{-1}$) using Tris-EDTA buffer solution. All primers and probes used in the study were described in supplementary information (Table S1), where the binding regions to the SARS-CoV-2 N gene are specified.

The study's human samples were provided by the Central Laboratory of Public Health of Pernambuco, Brazil (LACEN/PE). These biological specimens were obtained from nasopharyngeal and oropharyngeal swabs from patients with suspected COVID-19. To obtain SARS-CoV-2 viral RNA, 200 µL of the collected sample were transferred to an Eppendorf (1.5 mL) with 200 µL of lysis buffer, homogenized and incubated (15–30 °C, 10 min) and then another incubation (56 °C, 10 min). Then, QIAamp Viral RNA Mini Kit (QIAGEN®, Hilden, Germany) was used and followed the established procedure. Finally, we performed the RT-qPCR analysis after RNA extraction from real human samples. The biological material was collected with the patients' informed consent and the corresponding protocol was approved by the local ethics committee (process n° CAAE31093420.4.0000.5208).

### 2.3. PCR procedure for validation of clinical samples

As a reference to the electrochemical analyses, all samples were firstly assessed through RT-qPCR (Fig. S1). RT-qPCR tests for diagnosis of patients used in this study were carried out with comercial kit FDA EUA 2019-nCoV CDC, 500 rxn - IDT, USA (Catalog N° 10006606), following manufacturer's instructions. The commercial package FDA EUA 2019-nCo7V CDC is a validated and licensed kit for diagnosis, with assured sensitivity and specificity for the identification of SARS COV2 genetic material. The following primers and probes, N1, N2, N3 and RNase P, were evaluated through CDC functional test, using the Diagnostic Panel Instruction (List-of-Acceptable-Commercial-Primers-Probes.pdf (cdc.gov)). The authors

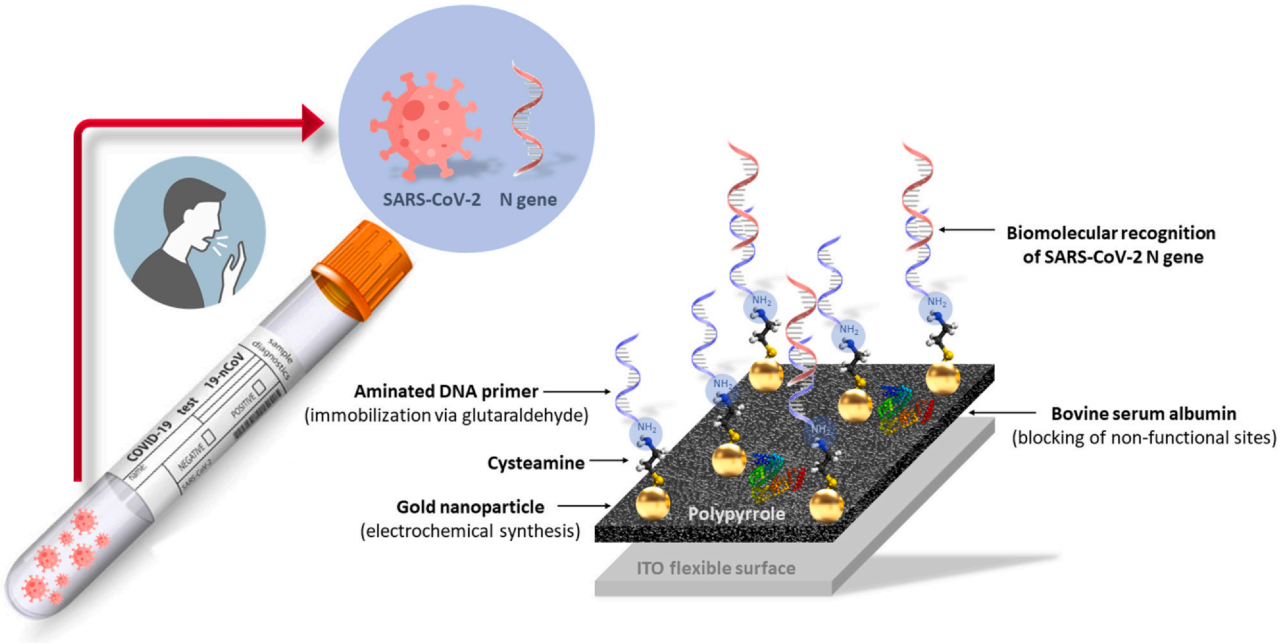


**Fig. 1.** Schematic representation of the assembly principle of the COVID-19 electrochemical sensing platform.

emphasize that frequently computer analysis is performed to verify whether mutations of new variants are detected in the sequence of the primers N1, N2 and N3 used. So far, no mutations have been found that invalidate the use of the kit for the diagnosis of patients positive for SARS-CoV- 2.

Briefly, following the manufacturer's instructions, 5 µL of the RNA samples were mixed with reagents, specific primers, and probes for SARS-CoV-2. The procedure was applied to four targets (N1, N2, N3, and RP). Cycling parameters were carried out as follows: reverse transcription (50 °C, 15 min), followed by 95 °C for 3 min for activation of the transcriptional reaction, and then 40 cycles (95 °C, 15 s) and 55 °C for 40 s corresponding to denaturation and annealing/extension, respectively. All tests were performed using a Real-Time PCR System (Applied Biosystems, USA) and analyzed through the QuantStudio Design and Analysis Software. After certifying the samples' positivity for SARS-CoV-2 infection, they were subjected to electrochemical analyses with the developed flexible miniaturized biosensor. Samples from healthy donors were also evaluated and used in the experiments.

### 2.4. Fabrication and assembly of the flexible sensor platform

The manufacturing process of the ITO electrode was depicted in Fig. 1. A sheet of ITO-coated PET slide (surface resistivity 60 Ω $sq^{-1}$) was used to obtain the working electrode. Firstly, after cutting the ITO into stripes (3 cm × 8 mm), they were washed and submitted to an ultrasound cleaning in acetone, ethanol, and deionized water. A polyvinyl chloride adhesive sheet composed of a circular hole (ϕ = 5 mm) was carefully applied to the ITO surface to achieve an identical and functional surface area to assemble the nanostructured sensor platform. The first step of the biosensor assembly consisted of the electrochemical polymerization of the PPy. The polymerization was carried out through 6 cycles of CV in the potential range of −0.4 to +1.0 V vs. Ag/AgCl (KCl 3M) and scan rate 100 mV $s^{-1}$, using the ITO strip as a working electrode immersed in an acidic solution containing 0.5 M HCl and 30 mM of pyrrole. Subsequently, the PPy surface was covered by GNP through electrochemical deposition, where PPy-ITO electrodes were immersed in a solution of 0.25 mM $HAuCl_4.3\ H_2O$. After, 10 cycles were performed in a CV potential range of +0.2 to −1.0 V, and scan rate 50 mV $s^{-1}$. The PPy-GNP electrode was then carefully rinsed with deionized water and dried in air. The third step relies on the chemisorption of Cys molecules onto GNP.

2 µL of an ethanolic solution of Cys (2.5 mM) was adsorbed onto the ITO electrode for 30 min, resulting in the PPy-GNP-Cys nanostructured platform. The immobilization of the COVID-19 DNA primer onto the ITO electrode was obtained by adsorbing 2 µL of 0.5% glutaraldehyde diluted in water for 10 min and then 2 µL of the specific oligonucleotide sequence (10 mM) for 15 min. Finally, aiming to block non-specific binding sites, 1% BSA in phosphate buffer saline (PBS; pH 7.4; 10 mM) was dropped onto the ITO biosensor, resulting in the PPy-GNP-Cys-Primer-BSA sensor platform.

### 2.5. Evaluation of the bioactivity and monitoring of SARS-CoV-2

The hybridization with complementary oligonucleotide sequences on the ITO sensor platform was performed using biological specimens of SARS-CoV-2 infected patients (cDNA samples). We used non-complementary oligonucleotide sequences and interfering molecules (glucose, glycine, ascorbic acid, and cholesterol) to evaluate the biosensor's selectivity. All biological samples were diluted in PBS (pH 7.4; 10 mM) and frozen until use. The procedure occurred applying 2 µL of the samples on the ITO electrode for 15 min and rinsed with deionized water to remove unbound molecules.

### 2.6. Electrochemical trials

Voltammetric and impedimetric analyzes were performed by a potentiostat/galvanostat Autolab PGSTAT 128N (Metrohm, The Netherlands) using NOVA 1.11 software. Electrochemical detection occurred in a three-electrode system immersed in a 10 mM $K_4[Fe(CN)_6]/K_3[Fe(CN)_6]$ (1:1) solution prepared in PBS (pH 7.4; 10 mM). The ITO flexible substrate was used as a working electrode. As reference electrode, we used Ag/AgCl (saturated 3 M KCl) and as counter electrode, we used platinum wire. CV was obtained at the potential range between −0.2 to +0.7 V (scan rate of 50 mV $s^{-1}$). Impedance data were recorded in a frequency range of 100 mHz to 100 kHz and amplitude of the applied sine potential of 10 mV.

### 2.7. Atomic force microscopy measurements

Topographic and morphological AFM images were obtained using an atomic force microscope SPM-9700 (Shimadzu, Japan) in a non-contact mode. All measurements were performed using cantilevers with silicon probe (Nanoworld, Japan). We used cantilevers with 42 N $m^{-1}$ spring constant and 300 kHz resonant frequencies. The images were obtained at room temperature with a scan rate of 1 Hz line $s^{-1}$ and scan area 5 × 5 µm. Gwyddion software was used to evaluate the images.

### 2.8. ATR-FTIR measurements

Fourier transform infrared spectroscopy (FTIR) measurements were performed from 650 $cm^{-1}$ to 4000 $cm^{-1}$ and a 2 $cm^{-1}$ resolution using an Agilent Cary 630 FTIR Spectrometer (Agilent Technologies, Rowville, Australia) with a diamond attenuated total reflectance (ATR) sampling accessory. The experiments were performed at 21 °C, and 50% relative humidity.

## 3. Results and discussion

### 3.1. AFM and ATR-FTIR analyses

AFM was used to investigate the functionalization and hybridization efficiency of the electrode. Fig. 2 illustrates the flexible electrode surface before and after exposure to positive and negative COVID-19 clinical samples. The topographic image of the electrochemically polymerized PPy film on the ITO substrate is shown in Fig. 2a. The polymeric coating shows a homogeneous morphology with isolated regions with a maximum height of 0.29 µm. According to literature reports, the observed roughness is characteristic of thinner PPy films with a nodular surface [11]. It is important to emphasize that this morphological profile is desirable for electrochemical biosensors since rough electrodes have high electroactive areas that improve sensitivity and increasing the number of active sites capable of recognizing the target molecules [12].

A notable change in the system morphology was observed after assembling the PPy-GNP-Cys-Primer-BSA sensor platform (Fig. 2b). The roughness peaks did not increase significantly (maximum height of 0.31 µm). The topographic profile is influenced by the particles' arrangement on the polymeric matrix, determining the roughness and average height of the system [13]. The transducer surface became rougher, and the morphological heterogeneity increased to a maximum height of 1.14 µm after interaction with SARS-CoV-2 positive human samples (Fig. 2c). The AFM analysis shows a dense layer on the sensor surface associated with the formation of double-stranded DNA (dsDNA) [14]. Therefore, the ability to detect viral genetic material is assumed. Fig. 2d shows no significant alteration of the sensor platform's roughness and heterogeneity during selectivity testing with non-complementary DNA molecules (maximum height of 0.47 µm).

In supplementary information, the ATR-FTIR measurements and characteristic peaks for the pristine ITO support and after PPy polymerization (Fig. S2 and Table S2), construction of the biosensing platform (Fig. S3), and hybridization process with positive sample were displayed (Fig. S4 and Table S3).

### 3.2. Electrochemical characterization of the sensor platform

CV and EIS were effective techniques to specify changes in transducer behavior after each modification step. Cyclic voltammograms are graphical representations of a current curve (I) as a potential function (E). The anodic and cathodic peak currents, Ipa and Ipc respectively, and voltammetric areas were calculated for each constituent of the biosensor (Table S4). From another perspective, the EIS spectra include a semicircular region at higher frequencies, characterizing the charge transfer resistance ($R_{CT}$) of the electrical double layer. Also, a linear part can be visualized at lower frequencies, indicating the diffusional process. In this work, the Randles equivalent circuit was used to adjust the impedance data. Randles equivalent circuit includes the resistance of the electrolytic solution (Rs), $R_{CT}$, constant phase element (CPE), and Warburg impedance ($Z_W$). The results obtained from the theoretical simulation with the Randles equivalent circuit were presented in Table S5.

Fig. S5 represents the potentiodynamic scans during the electropolymerization of PPy on flexible ITO substrate. Anodic oxidative polymerization was carried out in a potential range from −0.4 to +1.0 V in HCl solution at 0.5 M. The result revealed that the potential for initializing the electropolymerization of pyrrole was above 0.7 V versus Ag/AgCl. Consequently, a well-adhered homogeneous PPy black film was electrodeposited on the electrode surface, causing a

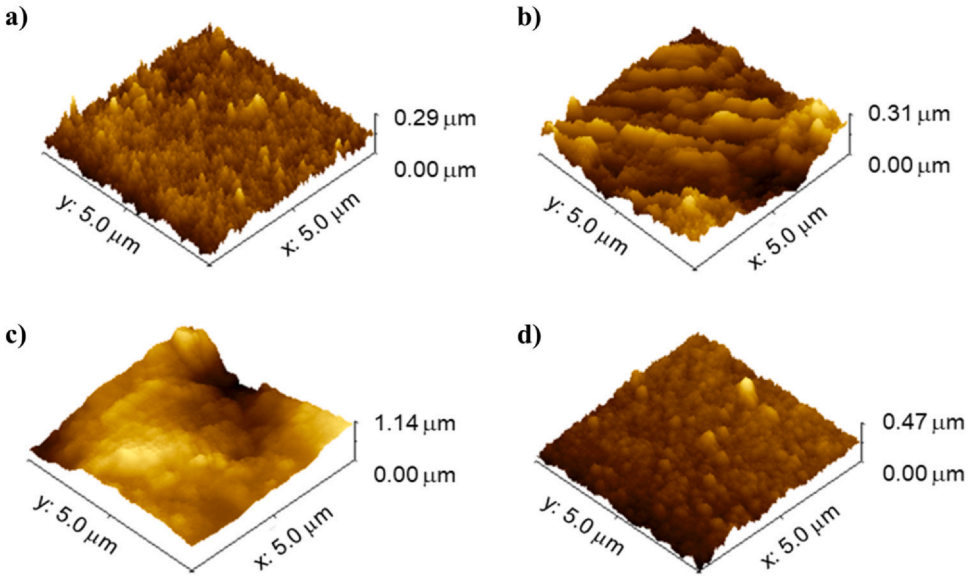


**Fig. 2.** AFM images of the PPy film (a), PPy-GNP-Cys-Primer-BSA film (b), PPy-GNP-Cys-Primer-BSA- SARS-CoV-2 sample film (c), and PPy-GNP-Cys-Primer-BSA-uninfected sample film (d).

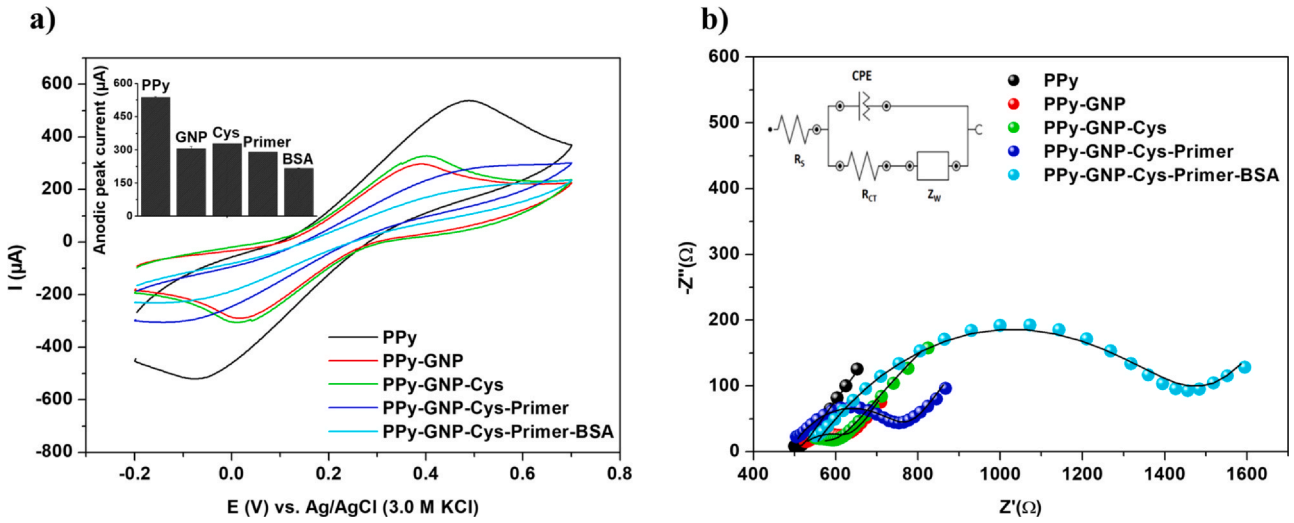


**Fig. 3.** Voltammetric (a) and impedimetric (b) characterization of each stage of construction of the flexible sensor platform. Inset: anodic peak currents obtained during the biosensor construction (a) and Randle's equivalent circuit used in the theoretical simulation of the impedance measurements (b). Three repetitions were performed for each methodological protocol, where the experimental data are presented as the mean values ± their standard deviation.

significant increase in anode current. The absence of a cathodic peak suggests the occurrence of an irreversible reaction of PPy electropolymerization. Thus, this behavior is associated with the immobilization of bulk anions in the polymeric matrix during doping [15]. Of note, six polymeric cycles were performed to obtain the polymeric matrix with a maximum current response. The decrease in polymer conductivity after six polymerization cycles is related to the increase in the PPy film thickness, which causes a lower diffusion rate [16]. We emphasize that 0.5 M HCl as dopant acid is a suitable medium to synthesize uniform polypyrrole films. Although it exhibits lower cycling stability compared to other electrolytes, the PPy film doped by HCl shows the longest charge-discharge time, highest capacitance and current density compared to other doping ions (eg, sulfates and phosphates) [17].

After the polymeric coating, the modifications of the working electrode were characterized by electrochemical measurements using the electrolytic solution containing 10 mM $K_4[Fe(CN)_6]/K_3[Fe(CN)_6]$ in PBS (pH 7.4; 10 mM) (Fig. 3). The PPy film exhibited a high current density (Ipa = 537.17 ± 2.98 μA) and a low impedimetric response with an electron transfer resistance of 0.04 ± 0.002 kΩ. This response is justified by forming the stable PPy film that features high conductivity, high electronic affinity, and a σ-π conjugate system that favors charge mobility throughout the molecule structure. Thus, these characteristics contribute significantly to improving the analytical performance and robustness of the biodetection systems. In addition, to access the approximate electroactive area of the electrode, we used the Randles-Sevcik equation [18].

$$Ip = \quad K.\, n^{\frac{3}{2}} \;.A.\, D^{\frac{1}{2}}.\, C.\, V^{\frac{1}{2}} \qquad (1)$$

Where K is the constant ($2.69 \times 10^5$), A is the electrode surface area in $cm^2$, D is the diffusion coefficient in $cm^2\ s^{-1}$ ($7.20 \times 10^{-6}\ cm^2$), n is the number of electrons transferred (=1), v is the scan rate in V/s ($0.100\ V\ s^{-1}$) and C is the probe molecule in the bulk solution ($10^{-6}\ mol\ cm^{-3}$). Thus, a surface area of $0.0029\ cm^2$ for PPy modified ITO was acquired.

Subsequently, the electroactive area for immobilization of biomolecules was improved by incorporating GNP into the polymer matrix [19]. A decrease in anodic and cathodic currents (Ipa = 304.85 ± 10.19 μA) was obtained after GNP electrosynthesis. Besides, an increase in the interfacial resistivity ($R_{CT}$ = 0.15 ± 0.001 kΩ) was observed. According to Li and Shi [20], PPy films contribute to the deposition of nanoparticles with reduced nanometric dimensions in a state of non-aggregation due to the expressive number of nucleation sites in the polymeric network. It is noteworthy that during electrosynthesis, GNPs can occupy PPy doping sites. Consequently, the redox reaction charge for the PPy-GNPs film may be lower compared to PPy [21].

In sequence, Cys molecules were self-assembled over GNP through the Au-thiol chemistry. The chemisorption process allows the formation of monomolecular films with a high degree of structural organization. In addition to the thiol termination, Cys molecules have an amino-functional group that provides covalent and stable adhesion of DNA sequences to maintain their conformational structure. The amino group present in Cys can be protonated, showing a positive electrical charge that attracts negatively charged electrolytes, such as $[Fe(CN)_6]^{3-/4-}$. This process favors the occurrence of oxidation-reduction reactions in regions adjacent to the electrode surface [22]. In this way, it was verified that the use of Cys as a spacer molecule increases current (Ipa = 327.92 ± 1.09 μA) and a decrease in charge transfer ($R_{CT}$ = 0.13 ± 0.002 kΩ), reflecting the proper assembly of the PPy-GNP-Cys nanostructured platform.

The redox peaks showed a further decrease by immobilizing single-stranded DNA (ssDNA) segments modified with the 5′ amino group (Ipa = 289.80 ± 1.04 μA). As expected, an increase in the $R_{CT}$ value was found ($R_{CT}$ = 0.29 ± 0.002 kΩ). The charge flow blockage is due to electrostatic repulsion between the electroactive anions in solution and the nucleotide structure's phosphate groups [23]. The nanostructured transducer's biofunctionalization was mediated by using the glutaraldehyde coupling agent. Thus, a Schiff bases' formation between two adjacent amino groups ($H_2N$-Cys and $H_2N$-primer) was obtained. The sensor system was incubated in a BSA solution to block non-functional electrode areas, resulting in an additional reduction in the electron transfer rate (Ipa = 217.07 ± 0.98 μA) and increased specific resistance ($R_{CT}$ = 0.99 ± 0.013 kΩ).

### 3.3. Analytical features of the sensor platform

The analytical performance of the PPy-GNP-Cys-Primer-BSA nanostructured system was evaluated through a biodetection assay using recombinant plasmids containing the nucleocapsid protein gene of SARS-CoV-2. The genomic concentrations of the analyzed samples were 800, 1000, 1333.33, 2000, and 4000 copies $\mu L^{-1}$. The voltammetry response decreases proportionally with the increase of the concentration of target DNA (Fig. 4a). The decrease in oxidation

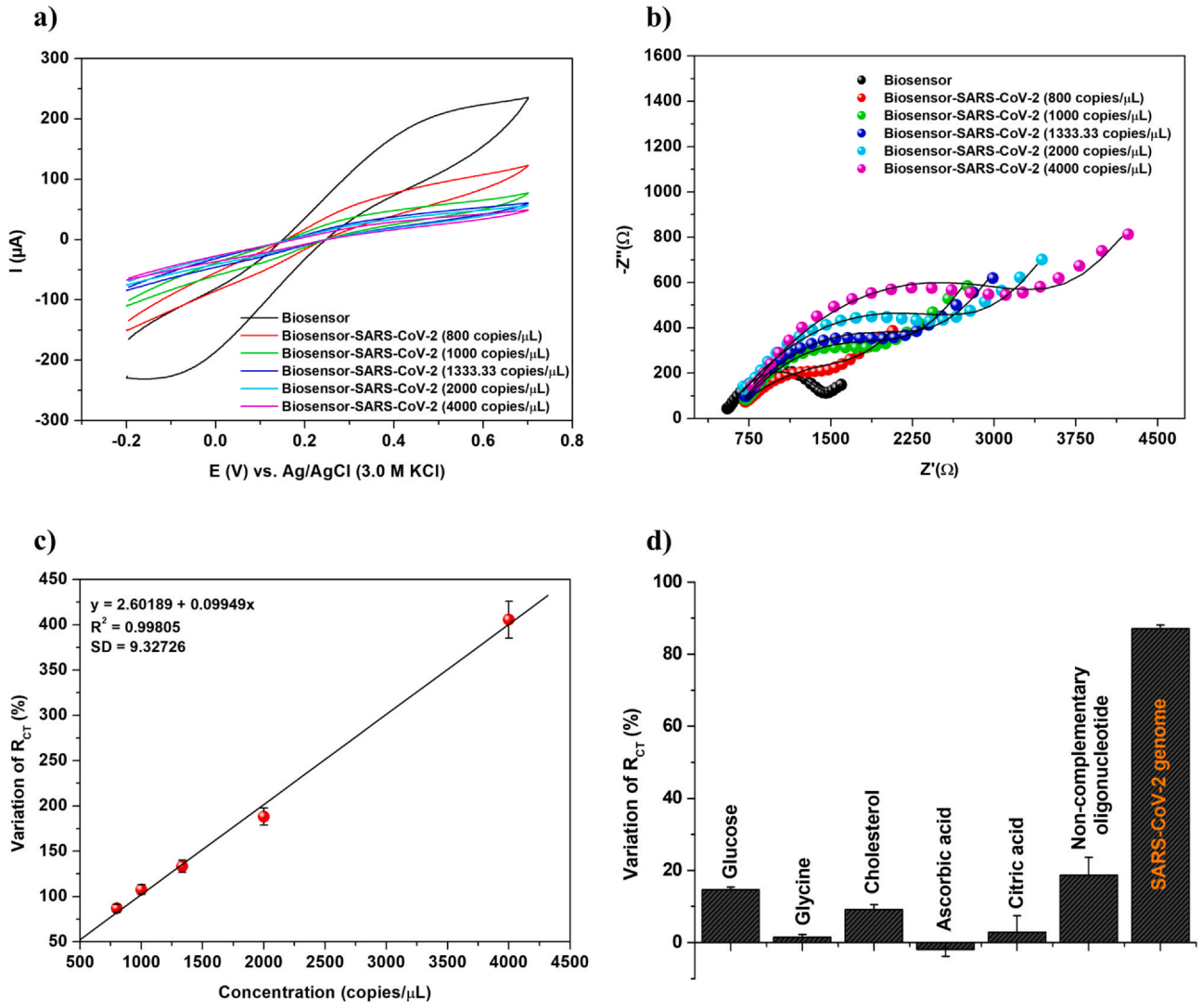


**Fig. 4.** Voltammetric records (a) and impedance spectra (b) for the flexible sensor platform exposed to different concentrations of the SARS-CoV-2 N gene in recombinant plasmids (DNA target: 800, 1000, 1333.33, 2000 and 4000 copies $\mu L^{-1}$). Calibration plot of the biossensor (c). Resistance variation for the selectivity study with non-complementary oligonucleotide sequence, glucose, glycine, cholesterol, and ascorbic acid (d). Three repetitions were performed for each methodological protocol, where the experimental data are presented as the mean values ± their standard deviation.

and reduction currents is related to the capture of the viral gene on biodevice's surface. The double-stranded DNA molecules (dsDNA) formed on the sensor layer have a negative global charge. This property hinders the transit of electrons between the transducer and the electroactive species. Consequently, changes in voltammetric signals are evidenced and associated with the detection mechanism [24].

EIS spectra demonstrate the electrochemical resistance against various viral nucleocapsid gene concentrations (Fig. 4b). Impedimetric measurements were positively correlated to the increase in the gene copy number. The bioanalytical tool's resistive properties gradually became more significant as the molecular target concentration increased, denoting the formation of hybrid DNA at the sensing interface. As mentioned earlier, this fact is due to the electrostatic repulsion between the negatively charged DNA strands and the negative charges of the $[Fe(CN)_6]^{3-/4-}$. Additionally, the biosensor's double layer impedance was represented by a constant phase element (CPE). From the CPE values presented in Table S5, it was observed that the measurements for the non-ideal capacitance progressively decreased after the exposure of the biosensor to samples with higher concentrations. This behavior may suggest less homogeneity of the sensing layer and reduced charge storage capacity due to the viral gene's interaction [25].

In Fig. 4c, we can see that the percentage variation of $R_{CT}$ ($\Delta R_{CT}$) is linear for the concentrations of the SARS-CoV-2 gene. The $\Delta R_{CT}$ is described as:

$$\Delta R_{CT}\,(\%) = \frac{R_{CT\,(Biosensor-viral\ genome)} - R_{CT\,(Biosensor)}}{R_{CT\,(Biosensor)}} \times 100 \quad (2)$$

where $R_{CT(Biosensor\text{-}viral\ genome)}$ is the value calculated after identification of the COVID virus genome and $R_{CT(Biosensor)}$ corresponds to the preliminary response of the PPy-GNP-Cys-Primer-BSA biosensor (Table S5). The measurement of this variable enabled the characterization of the analytical performance of the biosensitive platform. The linear regression equation was determined from the calibration plot as y = 2.60189 + 0.09949x with a determination coefficient ($R^2$) of 0.998. The *y* values correspond to $\Delta R_{CT}$ and the *x* values to the concentration (copies $\mu L^{-1}$) of the tested specimens.

The proposed nanostructured system showed a linear sensitivity range of 800–4000 copies $\mu L^{-1}$ with a standard deviation (SD) of 9.33 (S/N = 3). The proposed sensor obtained a limit of detection of 258.01

copies $\mu L^{-1}$, limit of quantification of 781.84 copies $\mu L^{-1}$, and sensitivity of 0.51 μA/copies $\mu L^{-1}$ $cm^2$. These parameters were calculated using the respective equations, 3.3σ/slope, 10σ/slope, and slope/(area of the electrode), where σ is the standard deviation of the blank measurement in three replicates and slope is the angular coefficient of the calibration plot (document ISO 11843) [26]. Adequate reproducibility was obtained with a relative standard deviation value of 1.31% for the nanostructured sensor system. The reproducibility was determined from the standard deviation's percentage value for three independent sensor systems produced with the same methodological protocol and experimental conditions in a single day. The repeatability was confirmed considering the relative standard deviation of less than 1% for all assays with the SARS-CoV-2 gene employing variable concentrations. To evaluate the repeatability, the analytical response of each sensor was tested at least three times in a single day. The biosensing platform' stability (PPy-GNP-Cys-Primer-BSA) was investigated over a period of 24 h under optimal storage conditions (storage temperature between 4 and 5 °C). The signal output ($R_{CT}$) at the stable stage was measured. The average resistance output of the biosensor was 989 Ω with a standard deviation of ± 1.29%. This impedimetric result suggests that the biosensor may exhibit prolonged stability over days. Considering the reusability, sensing interface architecture was regenerated after washing with 10 mM PBS solution (pH 7.4) at 94 °C. To ensure the reliability of the analytical result, the sensor system was reused up to three times. Electrochemical monitoring was performed in all cycles of use.

The selectivity of the nanostructured sensor was also assessed using the $\Delta R_{CT}$ intensity. Electrochemical experiments were performed with non-complementary oligonucleotide sequence and molecules commonly present in nasopharyngeal secretion (glucose, glycine, cholesterol, and ascorbic acid at a concentration of 0.5 ng $mL^{-1}$). It is emphasized that nasopharyngeal secretion contains 95% water, 2% mucin, 1% electrolytes, 1% lipids, and 1% of other proteins, such as albumin, immunoglobulins, lysozyme, kallikrein, and lactoferrin [27]. For this reason, the presence of glucose, glycine and cholesterol is inferred, in their free or bioconjugate form. In addition, ascorbic acid is the main antioxidant found in nasopharyngeal secretion [28]. Therefore, the mentioned biomolecules can be considered interfering elements in biosensing studies for SARS-CoV-2.

Fig. 4d shows the resistance variation for the selectivity study. The values measured for interfering species were relatively low ($\Delta R_{CT}$ = 1.52 ± 0.71–18.69 ± 5.00) as compared to the impedimetric signals obtained for the SARS-CoV-2 N gene ($\Delta R_{CT}$ = 86.87 ± 1.01–405.56 ± 5.00). It is noteworthy that the slight variations observed in the interfacial resistance are due to non-specific adsorption. Hence, our result suggests that the PPy-GNP-Cys-Primer-BSA platform has good selectivity, allowing the application of the biosensor in clinical trials.

### 3.4. Measurement of SARS-CoV-2 in clinical samples

The nanostructured flexible device's feasibility for the clinical diagnosis of COVID-19 was evaluated using human samples obtained from a nasopharyngeal swab. Molecular tests were processed with SARS-CoV-2-negative samples and others from patients at various stages of viral infection, as follow: initial (1st to 7th day of symptom onset), intermediate (7th to 14th day of symptom onset), and late (after the 14th day of symptom onset) (Fig. 5a). Positive samples for COVID-19 caused a more significant impedance variation ($\Delta R_{CT}$ of 56.39 ± 3.83–699.46 ± 12.84) than the negative samples ($\Delta R_{CT}$ of −10.55 ± 0.71–9.20 ± 1.01).

The analytical efficiency of the biosensor was performed in comparison to the RT-PCR technique. The relative variation of $R_{CT}$ was associated with the cycle threshold (CT) value of the RT-PCR analysis. The CT value can measure viral load in the clinical sample, directing the diagnostic interpretation and therapeutic decisions. An inversely proportional correlation between $\Delta R_{CT}$ values and CT values was found (Table S6). It is known that the lower the CT value, the greater the number of viral copies present in the clinical sample. In this sense, samples with higher viral expression (lower CT values) exhibited more significant impedimetric signals due to identifying a greater number of SARS-CoV-2 N gene sequences. The data were statistically analysed using kappa coefficient values. All values were significant ($p < 0.01$) for PCR method and biosensing platform used for SARS-CoV-2 detection in biological samples. Therefore, we demonstrated the ability of the electrochemical sensor to detect SARS-CoV-2 in cDNA samples.

The degree of surface coverage (θ) was used as a complementary parameter for diagnostic evaluation. θ values after exposure of the

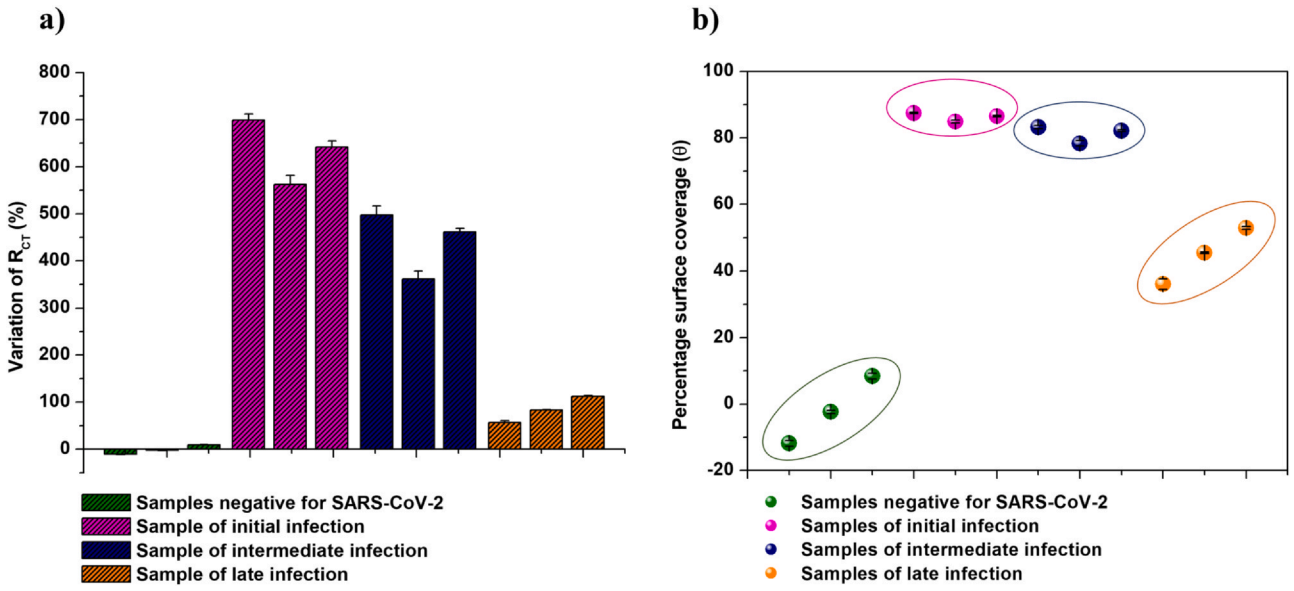


**Fig. 5.** Percentage variation of $R_{CT}$ (a) and degree of surface coverage (Θ) (b) for the flexible sensor platform exposed to samples from patients not infected with SARS-CoV-2 and samples from patients in early, intermediate and late stages of viral infection. Three repetitions were performed for each methodological protocol, where the experimental data are presented as the mean values ± their standard deviation.

**Table 1**
Analytical comparison between the biosensor presented in this work and the other electrochemical biosensors reported in the literature for the COVID-19 diagnosis.

| Sensing strategy | SARS-CoV-2 target | Analytical technique | Hybridization marker | Detection time | Detection range | Limit of detection | Limit of quantification | Sensitivity | Reference |
|---|---|---|---|---|---|---|---|---|---|
| ITO surface / PPy / GNP / Cys / Primer / BSA | N gene | CV and EIS | Label-free | 15 min | 800 copies $\mu L^{-1}$ to 4000 copies $\mu L^{-1}$ | 258.01 copies $\mu L^{-1}$ | 781.84 copies $\mu L^{-1}$ | 51 μA/copies $\mu L^{-1}$ $cm^2$ | This work |
| Gold electrode / Graphene nanoplatelets / thiol-modified ssDNA-capped gold nanoparticles *Four different antisense oligonucleotides were used. | N gene | Was applied a simple signal conditioning circuit | Label-free | 5 min | 585.4 copies $\mu L^{-1}$ to $5.854 \times 10^7$ copies $\mu L^{-1}$ | 6.9 copies $\mu L^{-1}$ | – | 231 (copies $\mu L^{-1}$)$^{-1}$ | [34] |
| Polyimide substrate / sputtered gold film / thiolated probe / biotinylated target / alkaline phosphatase-labeled streptavidin | N gene | *SWV | Alkaline phosphatase | 2 h | 0.1–10 nM | – | – | – | [35] |
| Biosensor based on isothermal rolling circle amplification | N and S genes | *DPV | Methylene blue and acridine orange | Less than 2 h | 1 copies $mL^{-1}$ to $1 \times 10^{10}$ copies $mL^{-1}$ | 1 copy $mL^{-1}$ | – | – | [31] |
| Gold electrode / DNA tetrahedron | RdRp gene | EIS and *ECL | $Ru(bpy)_3^{2+}$ | 1 h 15 min | 1 fM to 100 pM | 2.67 fM | – | – | [33] |
| Screen printing carbon electrode / nanocomposite of Au@$Fe_3O_4$ and thiolated capture probe / nanocomposite of graphene oxide functionalized with Au@ calixarene and toluidine blue *Supersandwich-type recognition strategy based on label probe and auxiliary probe. | ORF1ab gene | EIS and *DPV | Toluidine blue | 3 h | 1 pM to 10 aM | 200 copies $mL^{-1}$ | – | – | [32] |

*SWV: Square wave voltammetry
*DPV: Differential pulse voltammetry
*ECL: entropy-driven amplified electrochemiluminescence.

biomolecular system to clinical cDNA samples were calculated using the following equation:

$$\Theta(\%) = 1 - \frac{R_{CT\,(Biosensor)}}{R_{CT\,(Biosensor-viral\ genome)}} \times 100 \quad (3)$$

$R_{CT(Biosensor)}$ is the $R_{CT}$ value of the PPy-GNP-Cys-Primer-BSA system. $R_{CT(Biosensor\text{-}viral\ genome)}$ is the corresponding value for the biosensor against clinical samples. The surface coverage is related to the number of N gene sequences hybridized with a DNA primer on the sensor surface. The formation of hybrid DNA on the sensor layer increases the degree of surface coverage. Different θ values were calculated for samples of initial infection (θ = 84.90 ± 0.42–87.49 ± 0.20), intermediate infection (θ = 78.32 ± 0.80–83.24 ± 0.54), and late infection (θ = 36.03 ± 1.55–52.90 ± 0.39) (Fig. 5b). Lower θ values were found (θ = −11.80% ± 0.89–8.42% ± 0.85) for SARS-CoV-2-negative samples. These results denote the feasibility of the biosensor for target DNA assays in real samples. Of note, there are distinctive electrochemical responses for SARS-CoV-2-negative samples and patients in the early, intermediate, and late infection stages.

It is assumed that the electrochemical data are related to the circulating virus in the different periods of infectivity. In patients with COVID-19, a peak in viral load is commonly observed near the onset of symptoms (early infection stage) and gradually decreases. It is possible that asymptomatic COVID-19-positive individuals also exhibit high viral loads, contributing to the virus's spread [29]. The differentiation between the disease stages is essential to monitor the infection's evolution, therapeutic interventions and identify asymptomatic cases.

Nowadays, social distance and rapid diagnosis represent strategies for slowing the virus transmission and understanding the COVID-19 epidemiology. In this conjecture, electrochemical DNA biosensors represent an alternative approach to detect viral nucleic acids, contributing to the development of point-of-care-testing methods. Genetic screening devices are considered an ideal strategy for the COVID-19 diagnosis, particularly in the first to second week after infection when anti-SARS-CoV-2 antibodies cannot be detected (immune window) [30]. Table 1 summarizes the main electrochemical DNA biosensors reported in the literature for the SARS-CoV-2 detection. We compare our nanostructured genetic platform with other DNA biosensors based on electrochemical transduction.

Distinctively from other studies, the proposed biosensor displays electrochemical profiles correlated with the stage of viral infection, enabling the differential diagnosis for the SARS-CoV-2 infective phases. The biodetection device can quickly and quantitatively detect the viral gene in a small sample volume (only two µL of a sample is required). The sensor system exhibited interesting analytical performance parameters: comparable detection and quantification limits, high selectivity, specificity, and signal repeatability. Of note, most electrochemical tests depend on the analytical signal amplification using methylene blue [31], toluidine blue [32], acridine orange, and $Ru(bpy)_3^{2+}$ [33]. Here, the proposed biosensor is free of markers aiming to reduce the consumption of chemical reagents, analysis time, and, consequently, overall costs of the process. Finally, the flexible electrode technology used in the PPy-GNP-Cys-Primer-BSA biosensor allows more significant functional and design versatility in developing new emergency care tests. Although the clinical applicability of the electrochemical biosensor is promising, it should be noted that the technology is in development stage, being tested with a greater number of samples in accordance with analytical validation guidelines. It is expected to achieve the prototyping of the system to enable the accessibility, portability, and connectivity of the bioanalysis tool.

## 4. Conclusions

Conclusively, we have demonstrated the construction and characterization of a miniaturized flexible device based on conductive polymer and metallic nanoparticles for rapid and effective detection of nucleocapsid protein gene of SARS-CoV-2. The nanostructured platform shows a high reproducibility (variation of 1.31%), a large surface area, and signal transduction capability. The biomolecular recognition was achieved through surface chemistry, allowing for the stable and oriented immobilization of the DNA primer. The bioactivity assays were carried out with synthetic oligonucleotide samples and clinical cDNA samples, requiring reduced volume and without labeling agents. Our electrochemical biosensor showed significant specificity, selectivity, and sensitivity for SARS-CoV-2 with a limit of detection of 258.01 copies $\mu L^{-1}$ and a limit of quantification of 781.84 copies $\mu L^{-1}$. Different electrochemical profiles were obtained for the initial, intermediate, and late stages of the viral infection, showing the innovative performance of the PPy-GNP-Cys-Primer-BSA system. Where, the resistance variation values were significantly correlated with the CT values of the RT-PCR analyses. As a result of this finding, the electrochemical technique can be a viable alternative for SARS-CoV-2 differential diagnosis. Biosensors are alternative technologies for detecting new COVID-19 cases, contact tracing, and implementing treatments. Although the proposed biodetection system has not yet been tested in real nasal swab specimens without any purification and pre-treatment strategy, the results achieved were promising for the progressive development of an emergency care biosensor with scalability, ease of operation, compactness, and low cost.

## CRediT authorship contribution statement

**Karen Y.P.S. Avelino:** Methodology, Investigation, Formal analysis, Writing - Original Draft. **Gisele S. dos Santos:** Methodology, Investigation, Formal analysis, Writing - Original Draft. **Isaac A.M. Frías:** Methodology, Investigation, Formal analysis, Writing - Original Draft. **Alberto G. da Silva Júnior:** Methodology, Investigation, Formal analysis, Writing - Original Draft. **Michelly C. Pereira:** Methodology, Investigation, Conceptualization, Writing - Review & Editing, Supervision. **Maira G.R. Pitta:** Conceptualization, Writing - Review & Editing, Supervision, Funding acquisition. **Breno C. de Araújo:** Methodology, Investigation, Conceptualization, Writing - Review & Editing. **Abdelhamid Errachid:** Conceptualization, Writing - Review & Editing, Supervision, Funding acquisition. **Maria D.L. Oliveira:** Methodology, Investigation, Conceptualization, Writing - Review & Editing, Supervision, Funding acquisition. **César A.S. Andrade:** Conceptualization, Writing - Review & Editing, Supervision, Funding acquisition.

## Declaration of Competing Interest

The authors declare that they have no known competing financial interests or personal relationships that could have appeared to influence the work reported in this paper.

## Acknowledgments

This work was supported by the Brazilian National Council for Scientific and Technological Development/CNPq (grant numbers 314894/2018–7 and 314756/2018–3); Pernambuco State Foundation for Research Support, FACEPE-INOVA-IAM (grant number 0384–2.01/19); PROPESQ/UFPE; KardiaTool, H2020 (grant number 768686); and POC Allergies through the ERA PerMed program.

## Appendix A. Supporting information

Supplementary data associated with this article can be found in the online version at doi:10.1016/j.jpba.2021.114392.

## References


[1] Y. Ji, Z. Ma, M.P. Peppelenbosch, Q. Pan, Potential association between COVID-19 mortality and health-care resource availability, Lancet Glob. Health 8 (4) (2020) 480.

[2] P. Forster, L. Forster, C. Renfrew, M. Forster, Phylogenetic network analysis of SARS-CoV-2 genomes, Proc. Natl. Acad. Sci. U. S. A. 117 (17) (2020) 9241–9243.

[3] R.P. Rajkumar, COVID-19 and mental health: a review of the existing literature, Asian J. Psychiatry 52 (2020) 102066.

[4] H. Iqbal, K.D. Romero-Castillo, M. Bilal, R. Parra-Saldivar, The emergence of novel-coronavirus and its replication cycle-an overview, J. Pure Appl. Microbiol 14 (1) (2020) 13–16.

[5] L. Temime, M.-P. Gustin, A. Duval, N. Buetti, P. Crepey, D. Guillemot, R. Thiébaut, P. Vanhems, J.-R. Zahar, D.R. Smith, A conceptual discussion about the basic reproduction number of severe acute respiratory syndrome coronavirus 2 in healthcare settings, Clin. Infect. Dis. 72 (1) (2021) 141–143.

[6] F. Masotti, S. Cattaneo, M. Stuknytė, V. Pica, I. De Noni, Transmission routes, preventive measures and control strategies of SARS-CoV-2 in the food factory, Crit. Rev. Food Sci. Nutr. (2021) 1–12.

[7] Y. Pan, D. Zhang, P. Yang, L.L. Poon, Q. Wang, Viral load of SARS-CoV-2 in clinical samples, Lancet Infect. Dis. 20 (4) (2020) 411–412.

[8] R. Wölfel, V.M. Corman, W. Guggemos, M. Seilmaier, S. Zange, M.A. Müller, D. Niemeyer, T.C. Jones, P. Vollmar, C. Rothe, Virological assessment of hospitalized patients with COVID-2019, Nature 581 (7809) (2020) 465–469.

[9] S. Wang, Y. Pan, Q. Wang, H. Miao, A.N. Brown, L. Rong, Modeling the viral dynamics of SARS-CoV-2 infection, Math. Biosci. 328 (2020) 108438.

[10] E. Morales-Narváez, C. Dincer, The impact of biosensing in a pandemic outbreak: COVID-19, Biosens. Bioelectron. 163 (2020) 112274.

[11] S. Carquigny, O. Segut, B. Lakard, F. Lallemand, P. Fievet, Effect of electrolyte solvent on the morphology of polypyrrole films: application to the use of polypyrrole in pH sensors, Synth. Met. 158 (11) (2008) 453–461.

[12] Q. Zhu, Bo Liang, Y. Liang, L. Ji, C. Y.u, Ke Wu, T. Tu, H. Ren, B. Huang, J. Wei, Lu Fang, X. Liang, X. Ye, 3D bimetallic Au/Pt nanoflowers decorated needletype microelectrode for direct in situ monitoring of ATP secreted from living cells, Biosens. Bioelectron. 153 (2020) 112019.

[13] M. Fani, M. Rezayi, H.R. Pourianfar, Z. Meshkat, M. Makvandi, M. Gholami, S.A. Rezaee, Rapid and label-free electrochemical DNA biosensor based on a facile one-step electrochemical synthesis of rGO–PPy–(l-Cys)–AuNPs nanocomposite for the HTLV-1 oligonucleotide detection, Biotechnol. Appl. Biochem. (2020).

[14] M. Sajfutdinow, K. Uhlig, A. Prager, C. Schneider, B. Abel, D. Smith, Nanoscale patterning of self-assembled monolayer (SAM)-functionalised substrates with single molecule contact printing, Nanoscale 9 (39) (2017) 15098–15106.

[15] A.S. Liu, M.C. Bezerra, L.Y. Chao, Electrodeposition of polypyrrole films on aluminum surfaces from a p-toluene sulfonic acid medium, Mater. Res. 12 (2009) 503–507.

[16] S. Sayyah, S. Abd El-Rehim, M. El-Deeb, Electropolymerization of pyrrole and characterization of the obtained polymer films, J. Appl. Polym. Sci. 90 (7) (2003) 1783–1792.

[17] M. Zhang, A. Nautiyal, H. Du, J. Li, Z. Liu, X. Zhang, R. Wang, Polypyrrole film based flexible supercapacitor: mechanistic insight into influence of acid dopants on electrochemical performance, Electrochim. Acta 357 (2020) 136877.

[18] S. Kogikoski, C. Sousa, M. Liberato, T. Andrade-Filho, T. Prieto, F. Ferreira, A. Rocha, S. Guha, W. Alves, Multifunctional biosensors based on peptide–polyelectrolyte conjugates, Phys. Chem. Chem. Phys. 18 (4) (2016) 3223–3233.

[19] Y. Ye, J. Ji, F. Pi, H. Yang, J. Liu, Y. Zhang, S. Xia, J. Wang, D. Xu, X. Sun, A novel electrochemical biosensor for antioxidant evaluation of phloretin based on cell-alginate/L-cysteine/gold nanoparticle-modified glassy carbon electrode, Biosens. Bioelectron. 119 (2018) 119–125.

[20] Y. LI, G. SHI, Electrochemical growth of two-dimensional gold nanostructures on a thin polypyrrole film modified ITO electrode, J. Phys. Chem. B 109 (2005) 23787–23793.

[21] W. Chen, C.M. Li, P. Chen, C. Sun, Electrosynthesis and characterization of polypyrrole/Au nanocomposite, Electrochim. Acta 52 (8) (2007) 2845–2849.

[22] N. Wang, M. Lin, H. Dai, H. Ma, Functionalized gold nanoparticles/reduced graphene oxide nanocomposites for ultrasensitive electrochemical sensing of mercury ions based on thymine-mercury-thymine structure, Biosens. Bioelectron. 79 (2016) 320–326.

[23] H.-B. Xu, R.-F. Ye, S.-Y. Yang, R. Li, X. Yang, Electrochemical DNA nano-biosensor for the detection of genotoxins in water samples, Chin. Chem. Lett. 25 (1) (2014) 29–34.

[24] C. Srisomwat, P. Teengam, N. Chuaypen, P. Tangkijvanich, T. Vilaivan, O. Chailapakul, Pop-up paper electrochemical device for label-free hepatitis B virus DNA detection, Sens. Actuators B: Chem. 316 (2020) 128077.

[25] A.M. Nowicka, M. Fau, T. Rapecki, M. Donten, Polypyrrole-Au nanoparticles composite as suitable platform for DNA biosensor with electrochemical impedance spectroscopy detection, Electrochim. Acta 140 (2014) 65–71.

[26] P. Supraja, S. Tripathy, S.R.K. Vanjari, V. Singh, S.G. Singh, Electrospun tin (IV) oxide nanofiber based electrochemical sensor for ultra-sensitive and selective detection of atrazine in water at trace levels, Biosens. Bioelectron. 141 (2019) 111441.

[27] P.V. Tomazic, B. Darnhofer, R. Birner-Gruenberger, Nasal mucus proteome and its involvement in allergic rhinitis, Expert Rev. Proteom. 17 (3) (2020) 191–199.

[28] E. Borras, L. Schrumpf, N. Stephens, B.C. Weimer, C.E. Davis, E.S. Schelegle, Novel LC-MS-TOF method to detect and quantify ascorbic and uric acid simultaneously in different biological matrices, J. Chromatogr. B Anal. Technol. Biomed. Life Sci. 1168 (2021) 122588.

[29] Y. Hirotsu, M. Maejima, M. Shibusawa, Y. Nagakubo, K. Hosaka, K. Amemiya, H. Sueki, M. Hayakawa, H. Mochizuki, T. Tsutsui, Pooling RT-qPCR testing for SARS-CoV-2 in 1000 individuals of healthy and infection-suspected patients, Sci. Rep. 10 (1) (2020) 1–8.

[30] J. Kudr, P. Michalek, L. Ilieva, V. Adam, O. Zitka, COVID-19: a challenge for electrochemical biosensors, Trends Anal. Chem.: TRAC 136 (2021) 116192.

[31] T. Chaibun, J. Puenpa, T. Ngamdee, N. Boonapatcharoen, P. Athamanolap, A.P. O'Mullane, S. Vongpunsawad, Y. Poovorawan, S.Y. Lee, B. Lertanantawong, Rapid electrochemical detection of coronavirus SARS-CoV-2, Nature, Communications 12 (1) (2021) 1–10.

[32] H. Zhao, F. Liu, W. Xie, T.-C. Zhou, J. OuYang, L. Jin, H. Li, C.-Y. Zhao, L. Zhang, J. Wei, Ultrasensitive supersandwich-type electrochemical sensor for SARS-CoV-2 from the infected COVID-19 patients using a smartphone, Sens. Actuators B Chem. 327 (2021) 128899.

[33] Z. Fan, B. Yao, Y. Ding, J. Zhao, M. Xie, K. Zhang, Entropy-driven amplified electrochemiluminescence biosensor for RdRp gene of SARS-CoV-2 detection with self-assembled DNA tetrahedron scaffolds, Biosens. Bioelectron. 178 (2021) 113015.

[34] M. Alafeef, K. Dighe, P. Moitra, D. Pan, Rapid, ultrasensitive, and quantitative detection of SARS-CoV-2 using antisense oligonucleotides directed electrochemical biosensor chip, ACS Nano (2020).

[35] A. González-López, M.T.F. Abedul, Genosensor on gold films with enzymatic electrochemical detection of a SARS virus sequence, Laboratory Methods in Dynamic Electroanalaysis, Elsevier, 2020, pp. 213–220.